

**Investigation of n-type Doping Strategies for Mg₃Sb₂**

Journal:	<i>Journal of Materials Chemistry A</i>
Manuscript ID	TA-ART-04-2018-003344.R1
Article Type:	Paper
Date Submitted by the Author:	08-Jun-2018
Complete List of Authors:	Gorai, Prashun; Colorado School of Mines; National Renewable Energy Laboratory, Ortiz, Brenden; Colorado School of Mines Toberer, Eric; Colorado School of Mines; National Renewable Energy Laboratory Stevanovic, Vladan; Colorado School of Mines; National Renewable Energy Laboratory



Cite this: DOI: 10.1039/xxxxxxxxxx

Investigation of *n*-type Doping Strategies for Mg₃Sb₂[†]

Prashun Gorai,^{*a,b} Brenden R. Ortiz,^a Eric S. Toberer,^{a,b} and Vladan Stevanović^{*a,b}

Received Date

Accepted Date

DOI: 10.1039/xxxxxxxxxx

www.rsc.org/journalname

Recent, and somewhat surprising, successful *n*-type doping of Mg₃Sb₂ was the key to realizing high thermoelectric performance in this material. Herein, we use first-principles defect calculations to investigate different extrinsic *n*-type doping strategies for Mg₃Sb₂ and to reveal general chemical trends in terms of dopant solubilities and maximal achievable electron concentrations. In agreement with experiments, we find that Sb substitution is an effective doping strategy, with Se and Te doping predicted to yield up to $\sim 8 \times 10^{19} \text{ cm}^{-3}$ electrons. However, we also find that Mg substitution with trivalent (or higher) cations can be even more effective; in particular, the predicted highest achievable electron concentration ($\sim 5 \times 10^{20} \text{ cm}^{-3}$) with La as an extrinsic dopant exceeds that of Se and Te doping. Interstitial doping (Li, Zn, Cu, Be) is found to be largely ineffective either due to self-compensation (Li) or high formation energy (Zn, Cu, Be). Our results offer La as an alternative dopant to Te and Se and reinforce the need for careful phase boundary mapping in achieving high electron concentrations in Mg₃Sb₂.

1 Introduction

Intrinsic and extrinsic point defects play a critical role in determining properties of semiconductors including their dopability *i.e.* the achievable concentrations of free charge carriers of a certain type (electrons or holes). The dopability of a semiconductor is largely determined by the presence of native (intrinsic) defects and/or the properties of extrinsic dopants such as their solubilities at the growth conditions as well as their electronic properties.

In thermoelectrics, the concentrations of charge carriers needed to optimize the thermoelectric figure of merit, zT , are typically high (10^{19} - 10^{20} cm^{-3})^{1,2}. Therefore, understanding dopability is crucial to realize the full potential of thermoelectric materials. A prominent example of how native defects and growth conditions influence the dopability of materials and their thermoelectric performance is Mg₃Sb₂ (Figure 1). Historically, Mg₃Sb₂ was almost exclusively synthesized as a *p*-type material with a modest zT in the 0.2-0.4 range³⁻⁵. The main reason is the high volatility of Mg, which typically results in Mg-poor samples with significant concentrations of acceptor Mg vacancies⁶. More recently, *n*-type Mg₃Sb₂ was synthesized with excess Mg *i.e.*, under Mg-rich growth conditions, which suppresses the formation of Mg vacancies⁶⁻⁸, thereby resulting in relatively low intrinsic *n*-type doping. More importantly, this allows further enhancement of electron concentrations through extrinsic doping with Se and Te. Together with Bi alloying to reduce the lattice thermal conductiv-

ity, *n*-type Mg₃Sb₂ has demonstrated a high $zT > 1.5$. The experimental reports of high zT were preceded by computational predictions of promising thermoelectric performance of Mg₃Sb₂ for the assumed *n*-type doping^{9,10}. The good thermoelectric performance is attributed to the large number of carrier pockets (high band degeneracy) and small band effective masses in the conduction band, which result in high electrical conductivity and large Seebeck coefficient for electrons.

Using modern, first-principles defect calculations, we have previously investigated the role of native defects and growth conditions in the dopability of Mg₃Sb₂ and contributed to the understanding of the effectiveness of *n*-type doping with Te⁶. We found that the predominant defect changes from Mg vacancies under Mg-poor conditions to Mg interstitials under Mg-rich conditions; consequently, Mg₃Sb₂ changes its self-doping behavior from *p*-type to *n*-type. More importantly, the absence of Mg vacancies under Mg-rich conditions allows effective (uncompensated) extrinsic *n*-type doping with Te, and achievable free electron concentrations in excess of 10^{19} cm^{-3} . We revisit these prior findings in more detail in Section 3. While chalcogens (Se, Te) have been demonstrated to be effective *n*-type dopants, the doping behavior of other possible extrinsic *n*-type dopants and doping strategies beyond Sb substitution have not been explored so far.

In this study, we move beyond Te and use modern defect theory and defect calculations to investigate and compare various extrinsic *n*-type doping strategies for Mg₃Sb₂ including Sb substitution, Mg substitution and interstitial doping as illustrated in Figure 1. Additionally, we reveal general chemical trends for the various dopants, in terms of their solubilities and maximal achievable

^aColorado School of Mines, Golden, CO 80401. ^bNational Renewable Energy Laboratory, Golden, CO 80401. ^cNorthwestern University, Evanston, IL 60208. E-mail: pgorai@mines.edu, vstevano@mines.edu

[†] Electronic Supplementary Information (ESI) available

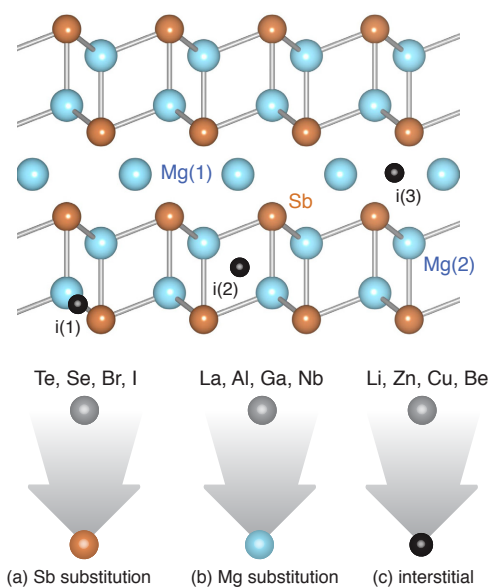


Fig. 1 Mg_3Sb_2 contains two unique Mg Wyckoff positions denoted by Mg(1) and Mg(2), and one unique Sb Wyckoff position. Favorable interstitial sites are marked by black spheres and denoted by i(1), i(2), and i(3). The crystal structure of Mg_3Sb_2 can be visualized as slabs of $[\text{Mg}_2\text{Sb}_2]^{2-}$ slabs intercalated with Mg^{2+} cations. Strategies for n -type doping include: (a) Sb substitution with mono- (Br, I) or di-valent (Se, Te) anions, (b) Mg substitution with tri- or higher-valent cations (La, Al, Ga, Nb), and (c) insertion of cation interstitials (Li, Zn, Cu, Be).

electron concentrations. The computational approach adopted in this work combines the supercell method with finite size corrections and band edge shifts from GW calculations¹¹, which has been demonstrated to provide reliable predictions of the energetics of native and extrinsic defects in semiconductors and the resulting charge carrier concentrations. In spite of its seemingly simple binary chemistry, the predicted carrier concentrations exhibit surprisingly complex behavior due to the presence of charge compensating defects and competing phases.

In total, we consider 11 extrinsic dopants following the three strategies: (1) Sb substitution - Se, Br, and I, (2) Mg substitution - La, Al, Ga, and Nb, and (3) interstitial insertion - Li, Zn, Cu, and Be. Our study reveals that, of all the dopants considered, La is the most effective extrinsic n -type dopant in Mg_3Sb_2 , and Mg substitution the most effective doping strategy. Mg substitution is even more effective than Sb substitution with Se and Te. The predicted maximal achievable electron concentrations for La doping ($\sim 5 \times 10^{20} \text{ cm}^{-3}$ at 900K) are almost an order of magnitude higher than that achieved with Te or Se doping. Other group-III elements (Al and Ga) are not as effective due to the counterintuitive self-compensation from dopant substitution of Sb. We also find Nb to be largely ineffective, which contradicts recent reports of Nb-doped Mg_3Sb_2 . Interstitial doping (Li, Zn, Cu, Be) is ineffective, either due to self-compensation (Li) or high formation energy of the interstitials (Zn, Cu, Be). Our results further support the need for careful phase boundary mapping⁶ in the dopant-Mg-Sb chemical potential phase space; for some dopants, due to the counterintuitive role of charge compensating defects,

the maximal free electron concentration may be achieved under less Mg-rich growth conditions. Finally, while this study is limited to n -type doping of Mg_3Sb_2 , the general principle of dopant phase boundary mapping can be extended to doping of other materials.

2 Methods

2.1 Calculation of Defect Energetics

To calculate the energetics of native point defects and extrinsic dopants in Mg_3Sb_2 , we perform first-principles defect calculations with density functional theory (DFT). Equation 1 describes how the formation energy ($\Delta H_{D,q}$) of a point defect D in charge state q is calculated:

$$\Delta H_{D,q} = (E_{D,q} - E_H) + \sum_i n_i \mu_i + qE_F + E_{corr} \quad (1)$$

The term $E_{D,q} - E_H$ represents the difference in the total energy of the defect-free host crystal with no net charge (E_H) and the host crystal with defect D in charge state q . The terms $\sum_i n_i \mu_i$ and qE_F account for the energy associated with exchange of elemental species and charge, respectively. The chemical potential of element i is denoted by μ_i and n_i is the number of atoms of element i added ($n_i < 0$) or removed ($n_i > 0$) to form the defect D . E_F is the Fermi energy. First-principles defect calculations are typically performed using periodically-repeated supercells, an approach that suffers from the artifacts arising from finite size effects. Additional artifacts arise from the limitations of the first-principles method *e.g.* underestimation of the band gap with standard functionals used in DFT. Various corrections to the defect formation energy are applied to alleviate these artifacts. These corrections are grouped into the E_{corr} term and briefly discussed in the following paragraphs. A more detailed description can be found elsewhere¹².

To calculate the total energies of the supercells, the generalized gradient approximation of Perdew-Burke-Ernzerhof (PBE)¹³ is utilized in the projector augmented wave (PAW) formalism as implemented in the VASP software package¹⁴. The defect energetics are calculated using the standard supercell approach¹². The total energies of defect supercells containing 90 atoms are calculated with a plane-wave energy cutoff of 340 eV and a Γ -centered Monkhorst pack k-point grid to sample the Brillouin zone. The defect supercells are relaxed following the procedure used in Ref. 15.

The elemental chemical potential μ_i can be expressed relative to the reference elemental phase as $\mu_i = \mu_i^0 + \Delta\mu_i$, where μ_i^0 is the reference chemical potential under standard conditions and $\Delta\mu_i$ is the deviation from the reference chemical potential. $\Delta\mu_i = 0$ corresponds to i -rich conditions. Inspired by the FERE approach¹⁶, the reference chemical potentials (μ_i^0) are established for elements in a family of materials (*e.g.* Mg-Sb, Mg-Sb-Te, Mg-Sb-Br) by fitting to a set of measured formation enthalpies of compounds in that material family. The bounds on $\Delta\mu_i$ for a given compound is set by the region of phase stability.

The underestimation of band gap in DFT is rectified by applying band edge shifts as determined from GW quasi-particle energy calculations. The following corrections are included in E_{corr} , fol-

lowing the methodology outlined in Ref. 12: (1) image charge correction for charge defects, (2) potential alignment correction for charged defects, (3) band filling correction for shallow defects, and (4) band gap correction for shallow acceptors/donors. The calculation setup and analyses are performed using a software package for automation of point defect calculations¹⁷.

Defect enthalpies of all vacancies, antisites, and interstitials in charge states $q = -3, -2, -1, 0, 1, 2,$ and 3 are calculated. Vacancies and antisites derived from all unique Wyckoff positions in the crystal structure are considered in the calculations. Likely interstitial sites are identified by Voronoi tessellation as implemented in the software package¹⁷. The position of the equilibrium Fermi energy, the corresponding defect concentrations, and the free carrier concentrations at a given temperature are calculated self-consistently by establishing the charge neutrality condition. The defect concentrations are calculated using the rigid band approximation, which is valid when the dopant concentrations are low such that the electronic structure, to a first approximation, remains unperturbed by doping. For effective dopants, the dopant concentrations are typically low and the rigid band approximation is likely to be valid, as demonstrated for Te doping of Mg_3Sb_2 .⁶

2.2 Synthesis and Doping

Mg_3Sb_2 and Li-doped Mg_3Sb_2 were synthesized under Mg-rich conditions, from Mg shavings (Alfa 99.9%), Sb shot (Alfa 99.9999%), and Li rod (99.8%). All sample preparations were performed in an argon glove box with oxygen and water concentrations <1 ppm. Mg shavings were purified by immersion in a solution of 200 mL reagent-grade anhydrous ethanol and 4 mL of concentrated HCl for 2 min, followed by an ethanol rinse and drying *en vacuo*. Elements were loaded into tungsten carbide ball mill vials with 3/4" tungsten carbide balls and milled for 2 h. Resulting powders were ground and sieved through a 106 μm mesh and densified *via* reactive hot-pressing under vacuum (<2 mTorr) at 600C.

3 Prior Findings

We have previously investigated the role of native defects and growth conditions in the dopability of Mg_3Sb_2 and predicted effective n -type doping with Te⁶. In this section, we revisit those prior findings for the purposes of contextualizing the results of various n -type doping strategies investigated in this work.

3.1 Self Doping

Native defects can result in self doping, as in the case of LiZnSb and SnSe. The calculated formation energies of native defects as a function of the Fermi energy (E_F) in Mg_3Sb_2 are shown in Figure 2 under Mg-poor and Mg-rich growth conditions (figures modified from Ref. 6). Defects with plots that have positive slopes are donors and negative slopes are acceptors. Neutral defects with zero slopes do not participate in the overall charge balance. Mg vacancies are the only acceptors in Mg_3Sb_2 while all of the other native defects are donors. The lowest energy configuration of the Mg interstitial is found to be in the octahedral site denoted by

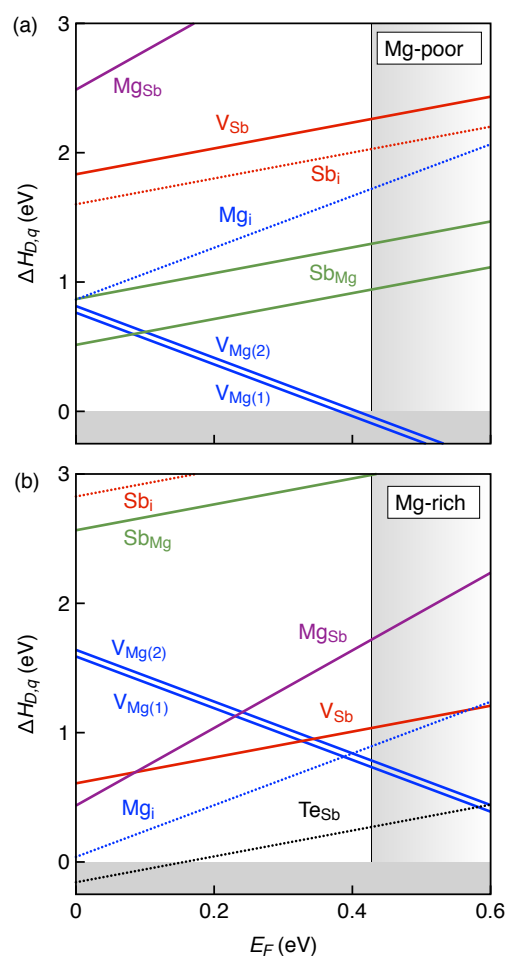


Fig. 2 Defect formation energy ($\Delta H_{D,q}$) as a function of the Fermi energy (E_F) for Mg_3Sb_2 grown under (a) Mg-poor and (b) Mg-rich conditions. E_F is referenced to the valence band edge. The shaded region on the right represents the conduction band. Under Mg-poor conditions, Mg_3Sb_2 is p -type while under Mg-rich conditions, Mg_3Sb_2 is n -type. Formation energy of substitutional Te_{Sb} under Mg-rich conditions is also shown in (b), where Te is an effective n -type extrinsic dopant.

$i(2)$ in Figure 1 while the Sb interstitial in the tetrahedral site denoted by $i(1)$. Mg_3Sb_2 has no other binary competing phases; consequently, the limit of Mg-poor condition corresponds to equilibrium with Sb ($\Delta\mu_{\text{Sb}} = 0$ eV) and Mg-rich condition to equilibrium with Mg ($\Delta\mu_{\text{Mg}} = 0$ eV). Due to the inherent volatility of Mg, historically, Mg_3Sb_2 has been grown under Mg-poor conditions, where the material is p -type. However, our recent work on phase boundary mapping⁶ shows that Mg_3Sb_2 is n -type when grown under Mg-rich conditions.

Mg-poor conditions

Under Mg-poor growth conditions, Mg vacancies are the dominant native defects (Figure 2a), a common trait of the 1-2-2 phases¹⁸. For Mg_3Sb_2 grown at 900K, the concentration of the acceptor defect V_{Mg}^{2-} is $\sim 6.7 \times 10^{18} \text{ cm}^{-3}$. We found that the donor antisite $\text{Sb}_{\text{Mg}(1)}$ is also the dominant defect under Mg-poor conditions with $\text{Sb}_{\text{Mg}(1)}^{1+}$ concentration of $\sim 7.0 \times 10^{18} \text{ cm}^{-3}$ (900 K). As a result of charge compensation between the donor V_{Mg} and ac-

ceptor $\text{Sb}_{\text{Mg}(1)}$, Mg_3Sb_2 is moderately *p*-type with hole concentration $\sim 6.4 \times 10^{18} \text{ cm}^{-3}$ at 900K. The predicted hole concentration is in fairly good agreement with experimental measurements^{3–5}. Within thermoelectrics, cation vacancies are well known as “electron killers” because they act as acceptors and limit the *n*-type dopability of materials, particularly in Zintl compounds such as ZnSb ¹⁹, and $\text{Ca}_5\text{Al}_2\text{Sb}_6$ ²⁰. The presence of large concentrations of Mg vacancies in Mg_3Sb_2 has been previously recognized¹⁸.

Mg-rich conditions

Under Mg-rich conditions, Mg interstitials are the dominant defects (Figure 2b) such that the E_F is pinned above the mid-gap and Mg_3Sb_2 is *n*-type. Sb vacancies (V_{Sb}) are also present in appreciable concentrations. For instance, at 900K growth temperature, the concentrations of Mg_i and V_{Sb} are $1.9 \times 10^{18} \text{ cm}^{-3}$ and $1.2 \times 10^{17} \text{ cm}^{-3}$, respectively. At the same temperature, the concentration of Mg vacancies is of the order of 10^{16} cm^{-3} . The predicted free electron concentration of $3.8 \times 10^{18} \text{ cm}^{-3}$ was found to be in good agreement with the measurements reported in the literature for samples grown with excess Mg⁶. Our results suggested that in Mg_3Sb_2 grown under Mg-rich conditions, Mg interstitials are indeed responsible for the *n*-type behavior.

In our prior study⁶, we concluded that under Mg-poor conditions, it is not possible to extrinsically dope Mg_3Sb_2 with large concentrations of electrons because of charge compensation with acceptor Mg vacancies. Under Mg-rich conditions (Figure 2b), the formation energy of Mg vacancies at the conduction band minima is $\sim 0.8 \text{ eV}$. Therefore, Mg_3Sb_2 can be further extrinsically doped with electrons provided the formation energy of the donor dopant is lower than $\sim 0.8 \text{ eV}$ at the conduction band minima.

3.2 Extrinsic Doping: Tellurium

The defect formation energy of the substitutional donor defect Te_{Sb} is shown in Figure 2(b), which is lower than that of Mg interstitial. We found that the Fermi energy is pinned inside the conduction band, resulting in degenerate *n*-type doping with $\sim 4 \times 10^{19} \text{ cm}^{-3}$ electrons (900K), and in excellent agreement with our experimental measurements of Te-doping⁶. Unlike *undoped* Mg_3Sb_2 grown under Mg-rich conditions where Mg interstitials are the dominant defects, in Te-doped Mg_3Sb_2 Mg interstitials are present in very low concentrations and do not play a role in *n*-type doping; in fact, the concentration of Mg vacancies exceed that of Mg interstitials.

4 Results

As described in the Introduction, the different *n*-type doping strategies (Figure 1) for Mg_3Sb_2 can be broadly classified into (a) anion substitution, (b) cation substitution, and (c) interstitial insertion. In this section, we computationally investigate a diverse set of 11 extrinsic dopants spanning the three different doping strategies. We consider 3 anion substitutions (Se, Br, I), 4 cation substitutions (La, Al, Ga, Nb), and 4 interstitial insertions (Li, Zn, Cu, Be). For each of these extrinsic dopants, the defect energetics are presented under Mg-rich conditions only (Figures 3, 4, 5). The defect energetics of Nb and Be doping can be found in the supplementary information.

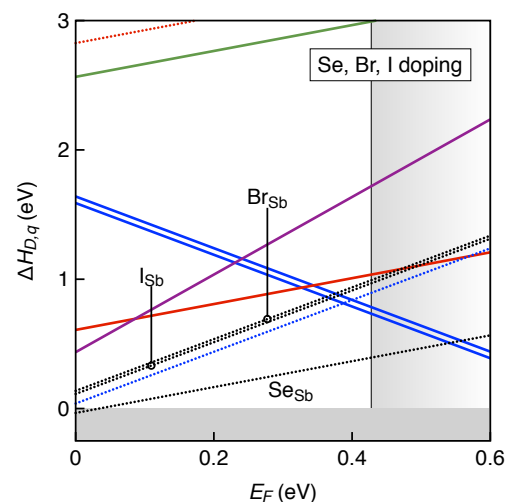


Fig. 3 Defect energetics of *n*-type doping of Mg_3Sb_2 by anion substitution under Mg-rich and most dopant-rich conditions. The native defects (Figure 2) are also shown for reference. Doping with chalcogenides (Se) and halides (Br, I). Substitutional Se_{Sb} , denoted by black dotted line, acts as an effective *n*-type dopant with formation energy lower than that of Mg interstitials. Substitutional halide dopants (Br_{Sb} , I_{Sb}), denoted by black dotted lines, exhibit formation energies similar to Mg_i and are not effective *n*-type dopants.

4.1 Anion Substitution

Anion substitution (Figure 1a) is the most common strategy that has been adopted for extrinsic *n*-type doping of Mg_3Sb_2 . The substituting anion must be di- or mono-valent since Sb is trivalent. Here, we consider di-valent chalcogenide (Se) and mono-valent halides (Br, I) as potential *n*-type dopants. In our calculations, we consider all possible charge states (-3, -2, -1, 0, 1, 2, 3) of the defect. The defect plots corresponding to each of these dopants are presented in Figure 3 for Mg-rich and the most extrinsic dopant-rich conditions as allowed by the phase stability of Mg_3Sb_2 in the ternary Mg-Sb-dopant phase space.

Selenium

The defect plot corresponding to the substitutional Se_{Sb} is shown in Figure 3. The formation energy of the donor Se_{Sb} is lower than that of Mg interstitials. As a result, the Fermi energy (E_F) is pinned inside the conduction band (shaded region on the right in Figure 3). Therefore, Se should be an effective *n*-type dopant that degenerately dopes Mg_3Sb_2 under Mg-rich conditions. The maximal free electron concentration is achieved under Mg-rich and the most dopant-rich conditions accommodated by the phase stability of Mg_3Sb_2 in the Se-Mg-Sb ternary phase space (Section 5). Indeed, Se has been experimentally found to be a good *n*-type dopant; Se-doped Mg_3Sb_2 exhibits relatively high zT of 1.23. The predicted electron concentration of $4 \times 10^{19} \text{ cm}^{-3}$ at 900K is in fairly good agreement with measurements, which provides further confidence in the fidelity of the first-principles defect calculations. When E_F is pinned inside the conduction band, the formation energy of Mg vacancies is lower than that of Mg interstitials. The concentration of Mg vacancies far exceeds Mg interstitials in Se-doped Mg_3Sb_2 , similar to our findings for Te-doped Mg_3Sb_2 in

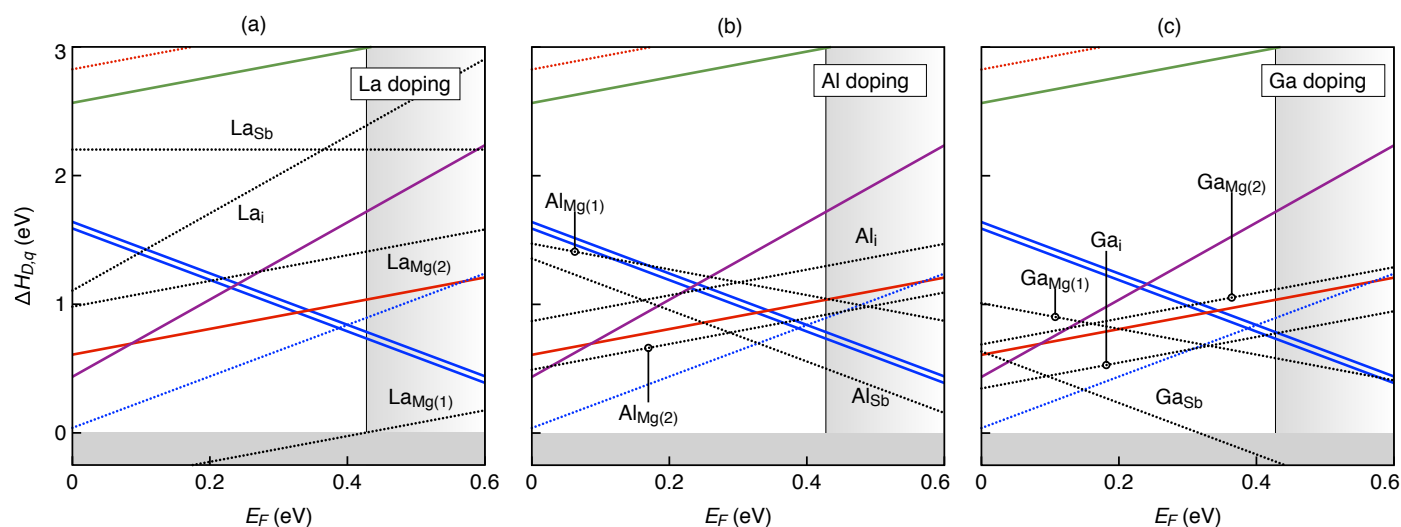


Fig. 4 Defect energetics of *n*-type doping of Mg_3Sb_2 by cation substitution under Mg-rich ($\Delta\mu_{\text{Mg}} = 0$ eV) and most dopant-rich conditions. The native defects (Figure 2) are also shown for reference. Doping with (a) La, (b) Al, (c) Ga. The defects corresponding to the extrinsic dopants are denoted by black dotted lines. La is found to be an effective dopant with predicted electron concentrations in excess of 10^{20} cm^{-3} (900K) while Al and Ga are ineffective due to electron compensation by dopant substitution of Sb. The low formation energy of Ga_{Sb} renders Mg_3Sb_2 *p*-type under Mg- and Ga-rich conditions.

our prior work.

Bromine, Iodine

Substitutional doping of the anion (Sb) site in Mg_3Sb_2 with monovalent anions such as halides has the distinct advantage that, in principle, for every halide ion two free electrons are generated when the halide is fully ionized. Compared to that, divalent chalcogenides can generate only one electron per chalcogenide ion. The disadvantage is that the formation energy ($\Delta H_{\text{D},q}$) as a function of the Fermi energy (E_{F}) increases with a slope of 2 as compared to a slope of unity for chalcogens (Eq. 1). The substitutional Br_{Sb} is a donor defect, as shown in Figure 3a, with formation energy that is comparable to that of Mg interstitials under Mg-rich growth conditions. As a result, the free electron concentration is only slightly enhanced by Br doping. The maximal free electron concentration of $4.4 \times 10^{18} \text{ cm}^{-3}$ at 900K is achieved under Mg-rich and most Br-rich conditions allowed by the phase stability of Mg_3Sb_2 (Section 5). The doping behavior of the substitutional I_{Sb} is almost identical to that of Br_{Sb} , with maximal free electron concentration of $4.6 \times 10^{18} \text{ cm}^{-3}$ at 900K.

The ineffectiveness of Br and I doping can be partly attributed to the high stability of the competing phases MgBr_2 and MgI_2 , which limits the solubility of Br and I in Mg_3Sb_2 . This is in contrast to Te and Se doping; despite the presence of stable competing phases of Mg chalcogenides (MgTe , MgSe), the energetics of Sb substitution are far more favorable. As a result, Te and Se are still effective *n*-type dopants.

4.2 Cation Substitution

Mg substitution with a tri- or tetra-valent cation could dope Mg_3Sb_2 *n*-type. Here, we consider La, Al and Ga as potential donor dopants. Recent reports of *n*-type doping with transition metals^{21,22} such as Nb, Hf, Ta, Co, and Fe prompted us to also

consider Nb doping. The defect plots corresponding to each of these dopants are presented in Figure 4 for Mg-rich and most dopant-rich conditions as accommodated by the phase stability of Mg_3Sb_2 in the ternary Mg-Sb-dopant phase space.

Lanthanum

The defect energetics of La doping, shown in Figure 4(a), suggests that La is an even more effective *n*-type dopant compared to Se and Te. As illustrated in Figure 1, there are two unique Wyckoff positions for Mg atoms in Mg_3Sb_2 : Mg(1) is the Mg located between the slabs and Mg(2) is the Mg that resides within the Mg_2Sb_2 slab. La preferentially substitutes Mg(1) over Mg(2); substitutional $\text{La}_{\text{Mg}(1)}$ is a low formation energy donor while $\text{La}_{\text{Mg}(2)}$ has significantly higher formation energy. The preferential La substitution of Mg(1) may be attributed to the large ionic size of La^{3+} that can be spatially accommodated between the Mg_2Sb_2 slabs rather than inside the slab by substituting Mg(2). The predicted free electron concentration at 900K (see Section 5) under Mg-rich and most La-rich conditions is $4 \times 10^{20} \text{ cm}^{-3}$, which is higher than that achieved by Se and Te doping. Several competing phases are present in the Mg-Sb-La phase space (Section 5) that limit the most dopant-rich conditions. In spite of the limitations of the dopant-rich conditions, similar to Se and Te doping, La is still an effective *n*-type dopant. We must note that the stability analysis (see Section 5) in the La-Mg-Sb chemical potential phase space does not take into account off-stoichiometric phases such as $\text{La}_4\text{Mg}_{4.5}\text{Sb}_7$, $\text{La}_3\text{Mg}_{4.6}\text{Sb}_6$, and $\text{La}_{4.89}\text{Mg}_{1.66}\text{Sb}_6$. These Sb-rich off-stoichiometric compounds are likely to form under Sb-rich conditions. However, the maximal achievable electron concentrations occur under Mg-rich conditions (see Section 5) and therefore, the exclusion of these off-stoichiometric phases will not affect the predicted maximal electron concentrations.

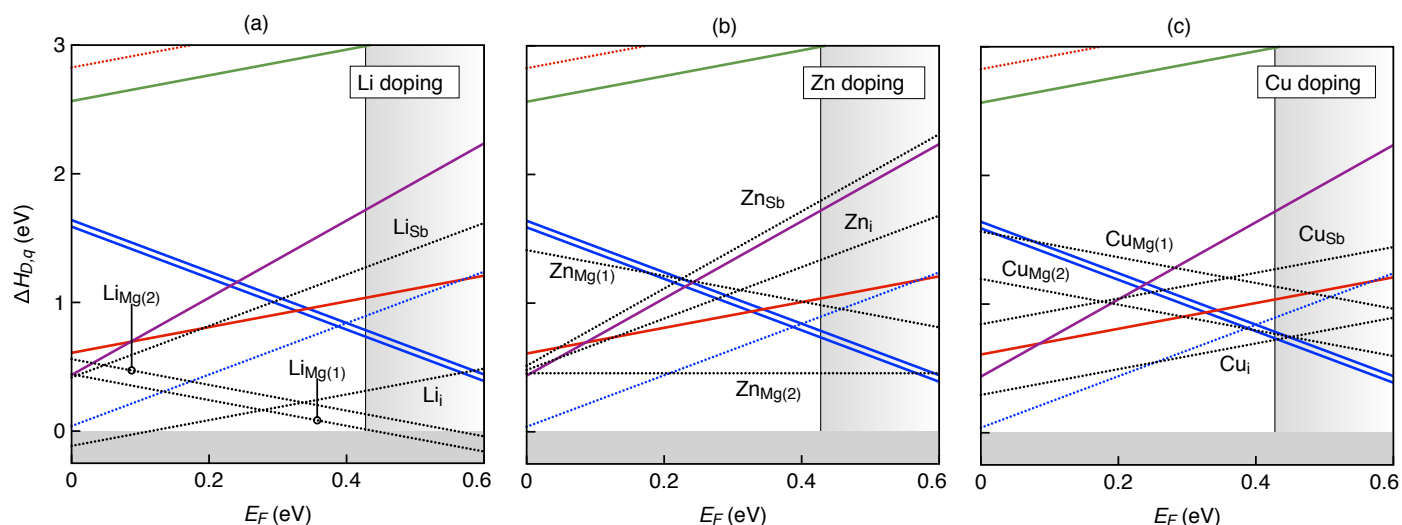


Fig. 5 Defect energetics of *n*-type doping of Mg_3Sb_2 by interstitial insertion under Mg-rich conditions. The native defects (Figure 2) are also shown for reference. Doping with (a) Li, (b) Zn, and (c) Cu. The defects corresponding to the extrinsic dopants are denoted by black dotted lines. While Li interstitials have low formation energy, the electrons are compensated by holes created by the acceptor Li_{Mg} , which also have low formation energy. Zn interstitials have high formation energy and therefore, not effective *n*-type dopant. Cu interstitials lead to a small increase in the electron concentration.

While Se and Te are demonstrably successful anion-site dopants, our prediction that La is a highly effective dopant provides a new cation-site dopant. Besides the higher free electron concentration that can be achieved with La doping, there may be additional benefits such as the lowering of the lattice thermal conductivity. It is known from phonon calculations²³ that the low-frequency optical modes ($\sim 3\text{--}4$ THz) in Mg_3Sb_2 are dominated by Mg(1) while the higher frequency optical modes ($\sim 6\text{--}8$ THz) are dominated by Mg(2). Preferential La substitution of Mg(1) combined with the pronounced Mg-La size and mass contrast can provide a source for significant point-defect scattering of the low-frequency optical modes. Given the effectiveness of La as a cation site *n*-type dopant, Sc and Y can also be expected to be effective dopants.

Aluminum, Gallium

Figure 4(b) presents the formation energy of defects resulting from Al doping of Mg_3Sb_2 under Mg-rich ($\Delta\mu_{\text{Mg}} = 0$ eV) and Al-rich ($\Delta\mu_{\text{Al}} = 0$ eV) conditions. Several defects are considered, as Al could conceivably substitute Mg and Sb as well as occupy interstitial sites. As expected, substitutional $\text{Al}_{\text{Mg}(2)}$ is a donor defect. However, the formation energy of $\text{Al}_{\text{Mg}(2)}$ at the conduction band minima is the same as Mg_i (~ 0.8 eV). Substitutional $\text{Al}_{\text{Mg}(1)}$ acts as an acceptor, which is contrary to our expectation. The different doping behavior of $\text{Al}_{\text{Mg}(1)}$ and $\text{Al}_{\text{Mg}(2)}$ is most likely related to the different ionicities of Mg(1) and Mg(2) as proposed in the literature²³. Nevertheless, the doping behavior of $\text{Al}_{\text{Mg}(1)}$ is inconsequential because of its high formation energy. More importantly, the low formation energy of the acceptor defect Al_{Sb} results in strong charge compensation, resulting in a slight decrease in the free electron concentration under Mg-rich and Al-rich conditions. For 900K growth temperature, the free electron concentration in Al-doped Mg_3Sb_2 is $3.3 \times 10^{18} \text{ cm}^{-3}$, compared to $3.8 \times 10^{18} \text{ cm}^{-3}$ in self-doped Mg_3Sb_2 . The charge compensation by Al_{Sb} can be

partly suppressed under Mg-poor (Sb-rich) conditions. As a result, the maximal achievable electron concentration at 900K is $7 \times 10^{18} \text{ cm}^{-3}$ (see Section 5). Al doping can lead to an increase in the electron concentration by a factor of only 2 compared to self-doping. Therefore, Al is not an effective *n*-type dopant.

The doping behavior of individual defects ($\text{Ga}_{\text{Mg}(1)}$, $\text{Ga}_{\text{Mg}(2)}$, Ga_{Sb} , Ga_i) in Ga-doped Mg_3Sb_2 (Figure 4c) is qualitatively similar to those in Al-doped Mg_3Sb_2 . Surprisingly, the acceptor defect Ga_{Sb} has a particularly low formation energy resulting in strong charge (electron) compensation. In fact, under Mg-rich ($\Delta\mu_{\text{Mg}} = 0$ eV) and Ga-rich ($\Delta\mu_{\text{Ga}} = 0$ eV) conditions, the equilibrium Fermi energy is below the mid-gap and Mg_3Sb_2 is doped *p*-type (Figure 4c). As in the case of Al doping, the charge compensation due to Ga_{Sb} may be suppressed under Mg-poor (Sb-rich) conditions, such that Mg_3Sb_2 is doped *n*-type, albeit with a decreased electron concentration compared to self-doping. The maximal achievable electron concentration is $2.6 \times 10^{18} \text{ cm}^{-3}$ at 900K (see Section 5).

Niobium

There are recent report of *n*-type doping of Mg_3Sb_2 with transition metals such as Nb, Hf, Ta, Co, and Fe^{21,22}. Within thermoelectrics, the use of transition metals as dopants is unusual and therefore, interesting. Transition metals often exhibit multiple oxidation states that could complicate doping. Consequently, the thermoelectrics community has generally avoided the use of these elements as dopants. Intrigued by the recent reports of *n*-type doping of Mg_3Sb_2 with Nb, we computationally investigate its doping behavior. The defect energetics of Nb doping are shown in Figure S1 (supplementary information) corresponding to Mg-rich ($\Delta\mu_{\text{Mg}} = 0$ eV) and most Nb-rich ($\Delta\mu_{\text{Nb}} = -0.08$ eV) conditions allowed by Mg_3Sb_2 phase stability (Figure S2). It is well known that transition metals such as Nb can exhibit different oxidation states, which is reflected in the different charge states adopted by

the substitutional $\text{Nb}_{\text{Mg}(1)}$ (neutral) and $\text{Nb}_{\text{Mg}(2)}$ (singly-charged donor). We find that both $\text{Nb}_{\text{Mg}(1)}$ and $\text{Nb}_{\text{Mg}(2)}$ have high formation energy. Our predictions suggest that Nb is not an effective n -type dopant, which is at odds with recent reports of Nb-doped n -type Mg_3Sb_2 . In light of these predictions, it would be prudent to revisit the hypotheses proposed in these recent studies.

4.3 Cation Interstitial

Anion and cation substitutions have been previously considered for n -type doping of Mg_3Sb_2 . A less explored route is via insertion of cation interstitials. Here, we explore 4 different cations (Li, Zn, Cu, Be) that are small in size and can be possibly accommodated as interstitials in the Mg_3Sb_2 crystal structure. We also report our experimental efforts of n -type doping with Li, which are in agreement with our theoretical predictions.

Lithium, Beryllium

Due to its small size, it is expected that Li interstitials will undergo facile insertion into the Mg_3Sb_2 structure. Indeed, Li interstitial (Li_i) is predicted to have a much lower formation energy than Mg interstitials (Figure 5a) and comparable in energy to substitutional dopants Se_{Sb} and Te_{Sb} . However, we find that acceptor defects, $\text{Li}_{\text{Mg}(1)}$ and $\text{Li}_{\text{Mg}(2)}$, also have low formation energies. Consequently, the electrons generated by Li interstitials are strongly compensated by holes generated by the acceptor defects. We predict that the maximal free electron concentration (at Mg-rich and most Li-rich conditions) is lower ($2.5 \times 10^{18} \text{ cm}^{-3}$ at 900K growth temperature) compared to self-doped Mg_3Sb_2 , rendering Li an ineffective n -type dopant.

Unlike other cation dopants considered in this study, Li-rich conditions ($\Delta\mu_{\text{Li}} = 0 \text{ eV}$) cannot be achieved because of the formation of a Li-rich competing phase, Li_3Sb (Section 5). However, this is not the limiting factor in n -type doping with Li. If the phase stability of Mg_3Sb_2 in the Mg-Sb-Li phase space could accommodate more Li-rich conditions, the formation energy of both Li_i and Li_{Mg} would be equally lower and the strong charge compensation would persist.

The energy differences between Li_{Mg} and Li_i are quite small, and thus the impact of Li doping is likely within the range of error within these calculations. To resolve this ambiguity, we synthesized Mg_3Sb_2 under Mg-excess conditions at 873K. The measured electron concentration in as-grown (Mg-rich) n -type Mg_3Sb_2 is approximately $8.5 \times 10^{17} \text{ cm}^{-3}$. Doping with 2% Li suppresses the electron concentration by more than an order of magnitude to approximately $3.7 \times 10^{16} \text{ cm}^{-3}$. Our measurements are qualitatively consistent with the predicted defect energetics and suggest that the charge compensation may be more severe than predicted.

In case of monovalent cation dopants such as Li, substitutional D_{Mg} (where D is the dopant) can cause electron compensation, rendering the interstitial doping ineffective. In contrast, divalent cation dopants may be less sensitive to such compensation because D_{Mg} can be expected to be neutral. This is confirmed for Be doping, shown in Figure S3 (supplementary information), where the substitutional Be_{Mg} is neutral. However, Be is not an effective n -type dopant because of the high formation energy of Be interstitials.

Zinc, Copper

We computationally assessed n -type doping via insertion of Zn and Cu interstitials as well as their corresponding substitutions on Mg and Sb sites (Figures 5b and 5c). Copper interstitials are fairly common in other thermoelectric materials such as Cu_{2-x}Se ²⁴, $\text{Cu}_{14}\text{Sb}_4\text{S}_{13}$ ²⁵. Zinc interstitials readily form in the thermoelectric material $\beta\text{-Zn}_4\text{Sb}_3$ ^{26,27}. Our defect calculations suggest that zinc is not an effective n -type dopant because the formation energy of Zn interstitials is fairly high compared to Mg interstitials (Figure 5b). Unlike Li, Zn is isoelectronic with Mg; consequently, the lower-energy substitutional defect $\text{Zn}_{\text{Mg}(2)}$ is charge neutral and does not cause charge compensation like Li_{Mg} .

The formation energy of Cu interstitials is slightly lower than that of Mg interstitials when E_F is close to the conduction band minima (Figure 5c) such that the maximal free electron concentration achieved (Mg-rich, Cu-rich conditions) is slightly higher than self-doping ($4.9 \times 10^{18} \text{ cm}^{-3}$ at 900K, compared to $3.8 \times 10^{18} \text{ cm}^{-3}$ in self-doped Mg_3Sb_2). The compensating defect $\text{Cu}_{\text{Mg}(2)}$ exhibits formation energy comparable to Cu interstitials near the conduction band minima. The +1 and -1 charge states of Cu_i and Cu_{Mg} suggests that Cu exists in +1 oxidation state in Mg_3Sb_2 .

5 Discussion

The free carrier type (electrons or holes) and their concentrations in a semiconductor depend on the growth conditions, besides other factors. The predicted free electron concentrations as functions of temperature for self-doped and extrinsically-doped Mg_3Sb_2 under Mg-rich and the most dopant-rich conditions (as accommodated by Mg_3Sb_2 phase stability) are shown in Figure 6. The phase stability of Mg_3Sb_2 represented in the binary Mg-Sb chemical potential space is bounded by Mg-rich/Sb-poor conditions ($\Delta\mu_{\text{Mg}} = 0 \text{ eV}$) on one end and Mg-poor/Sb-rich conditions ($\Delta\mu_{\text{Sb}} = 0 \text{ eV}$) on the other. In the composition space, Mg-rich

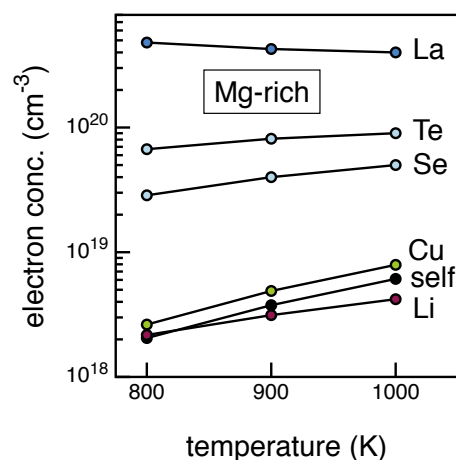


Fig. 6 Calculated free electron concentration as a function of temperature for self-doped and extrinsically doped Mg_3Sb_2 under Mg-rich ($\Delta\mu_{\text{Mg}} = 0 \text{ eV}$) and the most dopant-rich conditions *i.e.*, before secondary dopant-related phases start forming. For clarity, only 5 dopants (Li, Cu, Se, Te, La) are shown.

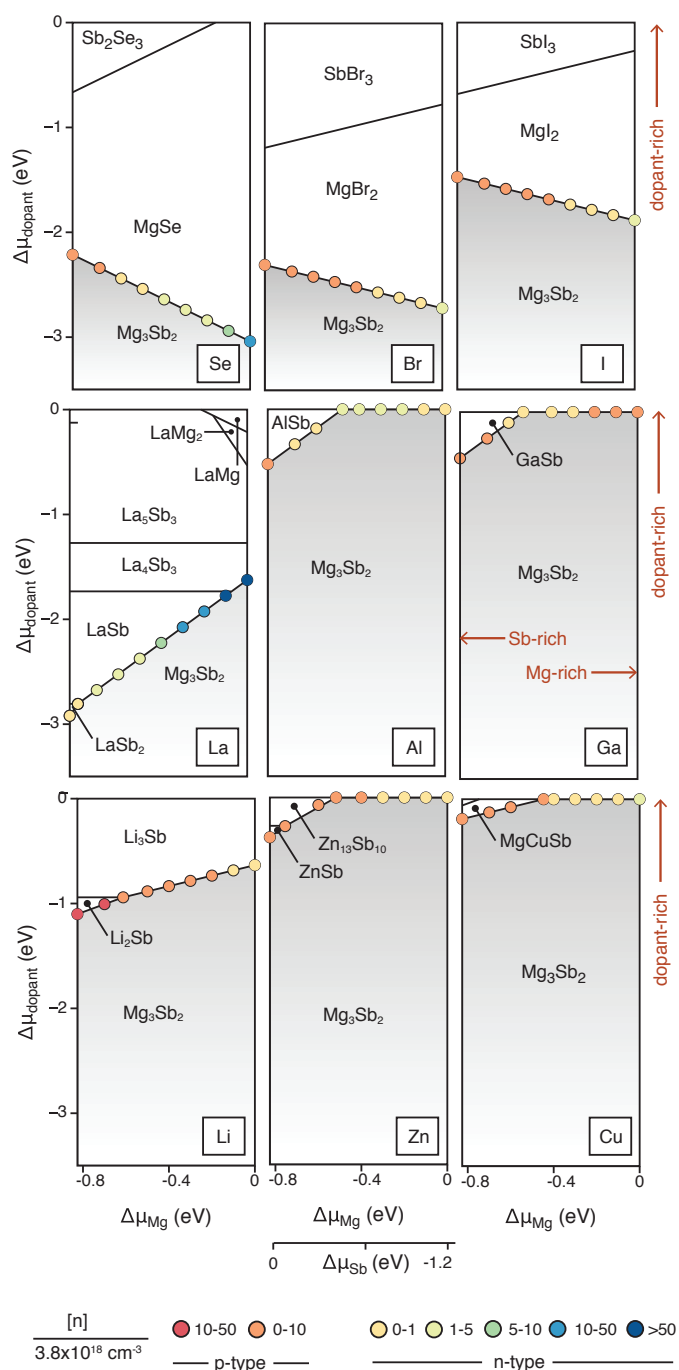


Fig. 7 Phase stability of Mg_3Sb_2 in the ternary dopant-Mg-Sb chemical potential phase space. The shaded area represents the region of phase stability of Mg_3Sb_2 . The x-axis is bounded by Mg-rich/Sb-poor ($\Delta\mu_{\text{Mg}} = 0$ eV, $\Delta\mu_{\text{Sb}} = -1.28$ eV) and Mg-poor/Sb-rich ($\Delta\mu_{\text{Mg}} = -0.83$ eV, $\Delta\mu_{\text{Sb}} = 0$ eV) conditions. The y-axis denotes $\Delta\mu_{\text{dopant}}$, ranging from dopant-rich (0 eV) and below. The markers at the Mg_3Sb_2 phase boundary are the free carrier concentrations calculated at 900K, normalized by the free electron concentration in self-doped n -type Mg_3Sb_2 grown under Mg-rich conditions ($3.8 \times 10^{18} \text{ cm}^{-3}$). Red and orange markers denote free hole concentrations while other colors free electron concentrations.

conditions correspond to Mg_3Sb_2 in equilibrium with Mg, and Mg-poor conditions correspond to equilibrium with Sb. Mg_3Sb_2

grown under Mg-poor conditions yield a p -type material^{3–5} while Mg_3Sb_2 grown under Mg-rich conditions is n -type^{6–8}. Therefore, to achieve the desired carrier type and concentrations in Mg_3Sb_2 , specific regions of the phase stability region have to be accessed. In practice, this is accomplished in experiments by performing phase boundary mapping⁶. For instance, Mg-rich conditions ($\Delta\mu_{\text{Mg}} = 0$ eV) are accessed by growing Mg_3Sb_2 with excess Mg such that trace amounts of Mg precipitates are present in equilibrium with Mg_3Sb_2 .

When extrinsically doped, one must consider the stability of Mg_3Sb_2 in the dopant-Mg-Sb ternary phase space. $\Delta\mu_{\text{dopant}} = 0$ eV corresponds to a dopant-rich condition or equilibrium with the dopant in elemental form. The range of dopant chemical potentials that can be accessed in the region of Mg_3Sb_2 phase stability depends on the presence of competing phases and their stability. Here, we examine the phase stability of Mg_3Sb_2 in the ternary dopant-Mg-Sb phase space for different dopants and the corresponding accessible range of dopant chemical potentials. The free carrier concentrations at the boundary of phase stability of Mg_3Sb_2 and dopant-related competing phases are presented. We emphasize the importance of dopant phase boundary mapping to achieve the desired carrier type and concentrations. Finally, based on the predicted carrier concentrations, we derive general guidelines for the various doping strategies.

5.1 Phase Stability and Carrier Concentrations

The region of phase stability of Mg_3Sb_2 in the ternary dopant-Mg-Sb phase space is presented in Figure 7 for the 9 different dopants (Se, Br, I, La, Al, Ga, Li, Zn, Cu) considered in this study. The phase stability of Mg_3Sb_2 in the Nb-Mg-Sb phase space is provided in Figure S2 in the supplementary information. The ternary phase space is represented by $\Delta\mu_{\text{Mg}}$ as the abscissa, ranging from Mg-rich condition ($\Delta\mu_{\text{Mg}} = 0$ eV) to Mg-poor ($\Delta\mu_{\text{Mg}} = -0.83$ eV). The abscissa also represents the corresponding $\Delta\mu_{\text{Sb}}$, ranging from -1.28 eV ($\Delta\mu_{\text{Mg}} = 0$ eV) to 0 eV ($\Delta\mu_{\text{Mg}} = -0.83$ eV). The ordinate, representing $\Delta\mu_{\text{dopant}}$, ranges from dopant-rich condition (0 eV) to dopant-poor ($-\infty$), which corresponds to the condition where no dopant is present.

For each of the 9 dopants shown in Figure 7, we have calculated the free carrier concentration (900K) at the phase boundary between Mg_3Sb_2 and the neighboring competing phases. The reasons for examining the carrier concentration at this boundary are two fold: (1) maximal carrier concentrations are achieved at this boundary, and (2) dopant phase boundary mapping can be performed in experiments by observing trace amounts of competing phases. The carrier concentrations are normalized by the free electron concentration in self-doped Mg_3Sb_2 ($3.8 \times 10^{18} \text{ cm}^{-3}$) grown under Mg-rich conditions (Figure 2b) at 900K. Electrons and holes are denoted by different colors.

For Se, Br, and I, the region of phase stability of Mg_3Sb_2 is limited to fairly dopant-poor conditions due to the presence of stable Mg chalcogenide (MgSe) and Mg halide (MgBr_2 , MgI_2) phases. In all three cases, the maximal electron concentration is achieved at the boundary where Mg-rich ($\Delta\mu_{\text{Mg}} = 0$ eV) conditions prevail.

As discussed earlier, Se is an effective n -type dopant and therefore, the maximal free electron concentration is $4 \times 10^{19} \text{ cm}^{-3}$ at 900K. Br and I are ineffective n -type dopants that only slightly increase free electron concentrations by a factor of ≈ 1.2 compared to self-doped n -type Mg_3Sb_2 .

There are several competing phases in the La-Mg-Sb chemical space that limit the stability of Mg_3Sb_2 to La-poor conditions, with maximum $\Delta\mu_{\text{La}} = -1.6 \text{ eV}$ (Figure 7). Given the low formation energy of the substitutional $\text{La}_{\text{Mg}(1)}$ (Figure 3a), the maximal electron concentration of $4 \times 10^{20} \text{ cm}^{-3}$ (at 900K) is achieved under Mg-rich and the most La-rich conditions. The predicted maximal electron concentration is an order of magnitude larger than that achieved by Se doping (Figure 6).

In case of Al and Ga, the dopant antimonides (AlSb, GaSb) are the only competing phases such that the region of phase stability of Mg_3Sb_2 can access dopant-rich conditions ($\Delta\mu_{\text{Al,Ga}} = 0 \text{ eV}$). Substitutional Al_{Sb} and Ga_{Sb} are strong charge (electron) compensating defects present in Al-doped and Ga-doped Mg_3Sb_2 , respectively (Figure 3a and 3b). As a result, the free carrier type and concentrations at the phase boundary exhibit interesting behavior. In Al-doped Mg_3Sb_2 , the maximal electron concentration is not achieved under Mg- and Al-rich conditions ($\Delta\mu_{\text{Al}} = 0 \text{ eV}$). Instead, it is achieved under slightly Mg-poor/Sb-rich conditions, where the formation energy of the compensating defect Al_{Sb} is higher than under Mg-rich/Sb-poor conditions. Specifically, the maximal electron concentration is achieved at the triple point where Al, AlSb, and Mg_3Sb_2 are in equilibrium. Since substitutional Ga_{Sb} has a lower formation energy than Al_{Sb} (Figure 3), Mg_3Sb_2 is doped p -type under Mg- and Ga-rich conditions ($\Delta\mu_{\text{Ga}} = 0 \text{ eV}$). Under slightly Mg-poor/Sb-rich conditions, the carrier type changes - Mg_3Sb_2 is doped n -type; the maximal free electron concentration is achieved at the triple point between Ga, GaSb, and Mg_3Sb_2 . Whilst the effect of strong charge compensating defects on the free carrier concentrations in Mg_3Sb_2 is subtle, the effect may be much more pronounced in other materials. In case of Nb (Figure S2), several competing Nb antimonide phases are present such that the most dopant-rich condition accessed by the phase stability of Mg_3Sb_2 is limited to $\Delta\mu_{\text{Nb}} = -0.08 \text{ eV}$. Nevertheless, given the high formation energy of substitutional Nb defects (Figure S1), the free carrier concentration remains unchanged compared to self-doped Mg_3Sb_2 .

The presence of stable Li_3Sb limits the most Li-rich condition to $\Delta\mu_{\text{Li}} = -0.63 \text{ eV}$. The maximal free electron concentration is achieved at Mg-rich ($\Delta\mu_{\text{Mg}} = 0 \text{ eV}$) and most Li-rich condition ($\Delta\mu_{\text{Li}} = -0.63 \text{ eV}$). Due to the strong charge compensation between the donor Li_i and acceptor Li_{Mg} (Figure 5a), the maximal free electron concentration is lower than self-doped n -type Mg_3Sb_2 . Interestingly, under Mg-poor/Sb-rich conditions ($\Delta\mu_{\text{Sb}} = 0 \text{ eV}$), the free hole concentration is $8.5 \times 10^{19} \text{ cm}^{-3}$ due to the low formation energy of the acceptor Li_{Mg} under those conditions; this suggest Li is a good p -type dopant under Sb-rich growth conditions. For Be, Zn and Cu, dopant-rich conditions ($\Delta\mu_{\text{dopant}} = 0 \text{ eV}$) are accessed by the phase stability of Mg_3Sb_2 . However, due to the high formation energy of the Be and Zn interstitial, the free carrier concentration remains unchanged compared to self-doped Mg_3Sb_2 . The maximal free electron concentration for Cu

doping, which is slightly higher than self-doped Mg_3Sb_2 (Figure 6), is achieved at Mg-rich and Cu-rich ($\Delta\mu_{\text{Cu}} = 0 \text{ eV}$) conditions.

We predict the free carrier concentrations from explicit defect calculations. Recently, Zhang *et al.*²⁸ proposed guiding principles for n -type doping of Mg_3Sb_2 based on the electronegativity difference ($\Delta\chi$) of the dopant (D) and Mg and Sb. According to the simple guiding principle, effective n -type doping on the anion site (Sb) is achieved for smaller dopant-Mg electronegativity differences ($\Delta\chi_{D-\text{Mg}}$) and on the cation site, for smaller dopant-Sb electronegativity differences ($\Delta\chi_{D-\text{Sb}}$). Using the Pauling electronegativity scale, $\Delta\chi_{D-\text{Mg}}$ is 1.24, 0.78, 1.65, and 1.35 for Se, Te, Br, and I, respectively. From our calculations, we find that I and Br are ineffective n -type dopants consistent with the guiding principle. However, our results suggest that the guiding principle cannot be extended to the cation site doping. For instance, $\Delta\chi_{\text{La}-\text{Sb}}$ is 0.95, which is much larger than $\Delta\chi_{\text{Ga}-\text{Sb}}$ (0.24), and $\Delta\chi_{\text{Cu}-\text{Sb}}$ (0.15). While useful, the guiding principle²⁸ simply assumes substitutional doping on the intended lattice site. Explicit defect calculations presented in this work reveal that cation site doping is more complex. For example, strong charge compensation may occur due to unexpected, facile substitution on the anion site, as in the case of Ga doping. Explicit defect calculations, in lieu of guiding principles, are further necessitated for interstitial doping. Again, we observe the significant role of charge compensation even for interstitial doping e.g. Li doping ($\Delta\chi_{\text{Li}-\text{Sb}} = 1.07$).

6 Conclusions

In this work, we have computationally assessed three different n -type doping strategies for Mg_3Sb_2 , including anion substitution, cation substitution, and interstitial insertion. Out of the 11 possible dopants considered, Se (and previously Te) is found to be the most effective for anion substitution and La for cation substitution. Interstitial doping with Li, Zn, Cu, and Be is found to be ineffective for n -type doping; however, Li is identified as a good p -type dopant. The following guidelines emerge from this study for the different n -type doping strategies:

- Anion substitution: Maximal electron concentration is achieved under Mg-rich and most dopant-rich conditions accessed by the phase stability of Mg_3Sb_2 .
- Cation substitution: Due to the presence of low formation energy electron-compensating defects, the maximal electron concentration is achieved under slightly Mg-poor/Sb-rich conditions. If the compensating defects have high formation energy, the maximal electron concentration is achieved under Mg-rich and most dopant-rich conditions. Of all the elements considered, La is found to be the most effective n -type dopant and Mg substitution the most effective doping strategy in terms of the achievable electron concentrations.
- Interstitial insertion: Cation interstitials maximize the electron concentration under Mg-rich and most dopant-rich conditions. In case of monovalent cation dopants, electron compensation by low formation energy substitutional D_{Mg} , where D is the dopant, can be suppressed under Mg-rich con-

ditions. In contrast, divalent cation dopants are less sensitive to this concern because D_{Mg} can be expected to be neutral.

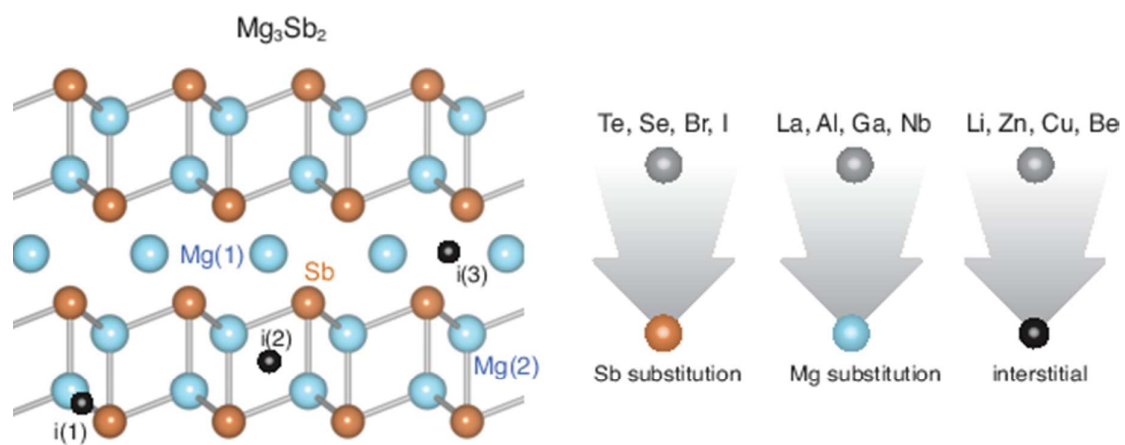
Traditionally, semiconductors are doped to *enhance* the free carrier concentrations, as in the case of Mg_3Sb_2 . However, in degenerately self-doped semiconductors, there may be a need to *lower* the free carrier concentration in order to maximize zT . This can be achieved by doping that introduces the desired charge compensating defects combined with dopant phase boundary mapping.

Acknowledgements

We thank G. Jeffrey Snyder for fruitful discussions. We acknowledge support from NSF DMR program, grant no. 1729594. The research was performed using computational resources sponsored by the Department of Energy's Office of Energy Efficiency and Renewable Energy and located at the NREL.

References

- 1 G. J. Snyder and E. S. Toberer, *Nat. Mater.*, 2008, **7**, 105.
- 2 P. Gorai, V. Stevanovic and E. S. Toberer, *Nature Reviews Materials*, 2017, **2**, 1–16.
- 3 V. Ponnambalam and D. T. Morelli, *J. Electron. Mat.*, 2013, **42**, 1307–1312.
- 4 C. L. Condon, S. M. Kauzlarich, F. Gascoin and G. J. Snyder, *J. Solid State Chem.*, 2006, **179**, 2252–2257.
- 5 A. Bhardwaj and D. K. Misra, *RSC Adv.*, 2014, **4**, 34552–34560.
- 6 S. Ohno, K. Imasato, S. Anand, H. Tamaki, S. D. Kang, P. Gorai, H. K. Sato, E. S. Toberer, T. Kanno and G. J. Snyder, *Joule*, 2017, **2**, 141.
- 7 H. Tamaki, H. K. Sato and T. Kanno, *Adv. Mater.*, 2016, **28**, 10182–10187.
- 8 J. Zhang, L. Song, A. Mamakhel, M. R. V. Jørgensen and B. B. Iversen, *Chem. Mater.*, 2017, **29**, 5371–5383.
- 9 J. Zhang, L. Song, S. H. Pedersen, H. Yin, L. T. Hung and B. B. Iversen, *Nature Comm.*, 2017, **8**, 1–8.
- 10 J. Yan, P. Gorai, B. Ortiz, S. Miller, S. A. Barnett, T. Mason, V. Stevanovic and E. S. Toberer, *Energy Environ. Sci.*, 2015, **8**, 983.
- 11 H. Peng, D. O. Scanlon, V. Stevanovic, J. Vidal, G. W. Watson and S. Lany, *Phys. Rev. B*, 2013, **88**, 115201.
- 12 S. Lany and A. Zunger, *Phys. Rev. B*, 2008, **78**, 235104.
- 13 J. P. Perdew, K. Burke and M. Ernzerhof, *Phys. Rev. Lett.*, 1996, **77**, 3865.
- 14 G. Kresse and J. Furthmüller, *Phys. Rev. B*, 1996, **54**, 11169.
- 15 B. Ortiz, P. Gorai, V. S. Stevanović and E. S. Toberer, *Chem. Mater.*, 2017, **29**, 4523.
- 16 V. Stevanović, S. Lany, X. Zhang and A. Zunger, *Phys. Rev. B*, 2012, **85**, 115104.
- 17 A. Goyal, P. Gorai, H. Peng, S. Lany and V. S. Stevanović, *Comp. Mat. Sci.*, 2016, **130**, 1.
- 18 G. S. Pomrehn, A. Zevalkink, W. G. Zeier, A. van de Walle and G. J. Snyder, *Angewandte Chemie*, 2014, **53**, 3422–3426.
- 19 L. Bjerg, G. K. H. Madsen and B. B. Iversen, *Chem. Mater.*, 2012, **24**, 2111–2116.
- 20 E. S. Toberer, A. Zevalkink, N. Crisosto and G. J. Snyder, *Adv. Func. Mater.*, 2010, **20**, 4375–4380.
- 21 J. Mao, J. Shuai, S. Song, Y. Wu, R. Dally, J. Zhou, Z. Liu, J. Sun, Q. Zhang, C. dela Cruz, S. Wilson, Y. Pei, D. J. Singh, G. Chen, C.-W. Chu and Z. Ren, *Proc. Nat. Acad. Sci.*, 2017, **114**, 10548–10553.
- 22 J. Shuai, J. Mao, S. Song, Q. Zhu, J. Sun, Y. Wang, R. He, J. Zhou, G. Chen, D. J. Singh and Z. Ren, *Energy Environ. Sci.*, 2017, **10**, 799–807.
- 23 J. ichi Tani, M. Takahashi and H. Kido, *Physica B: Condensed Matter*, 2010, **405**, 4219–4225.
- 24 H. Liu, F. Xu, L. Zhang, W. Zhang, L. Chen, Q. Li, C. Uher, T. Day and G. J. Snyder, *Nature Mat.*, 2012, **11**, 422–425.
- 25 D. P. Weller, D. L. Stevens, G. E. Kunkel, A. M. Ochs, C. F. Holder, D. T. Morelli and M. E. Anderson, *Chem. Mater.*, 2017, **29**, 1656–1664.
- 26 E. S. Toberer, K. A. Sasaki, C. R. I. Chisholm, S. M. Haile, W. A. Goddard and G. J. Snyder, *Physica Status Solidi*, 2007, **1**, 253–255.
- 27 F. Cargnoni, E. Nishibori, P. Rabiller, L. Bertini, G. J. Snyder, M. Christensen, C. Gatti and B. B. Iversen, *Chemistry - Eur. J.*, 2004, **10**, 3861–3870.
- 28 Z. Jiawei, S. Lirong, B. K. Andersen, J. M. R. Vogel and I. B. Brummerstedt, *Adv. Energy Mater.*, 1702776.



Computational investigation of n-type doping strategies for Mg_3Sb_2 reveals new cationsite dopants.